Supplemental material for "Quantum transport in Sierpinski carpets"

Edo van Veen,[1] Shengjun Yuan,[1] Mikhail I. Katsnelson,[1] Marco Polini,[2] and Andrea Tomadin[3]

[1] *Radboud University, Institute for Molecules and Materials, NL-6525 AJ Nijmegen, The Netherlands*
[2] *Istituto Italiano di Tecnologia, Graphene Labs, Via Morego 30, I-16163 Genova, Italy*
[3] *NEST, Istituto Nanoscienze-CNR and Scuola Normale Superiore, I-56126 Pisa, Italy*

In this Supplemental Material file we detail the geometry of the fractal samples which we discuss in the main text. Moreover, we present some results concerning the robustness of phase-coherent transport in the Sierpinski carpet with respect to disorder. We consider both localized and smoothly varying disorder. Finally, we explain in detail how we apply the box-counting algorithm to obtain an estimate of the fractal dimension of a quantum conductance graph as a function of energy.

Geometry of the Sierpinski carpet

Fig. 1 shows several Sierpinski carpets (SCs) with $\mathcal{N} = 3$ and $\mathcal{L} = 2$ (as defined in the caption of Fig. 1 of the main text) but different underlying lattices, for central [a), c), and e)] and diagonal [b), d), and f)] lead positions. Panels a) and b) show a triangular-lattice SC with $m = 2$ and $n = 33$. c) and d) show a square-lattice SC with $m = 3$ and $n = 54$. e) and f) show a hexagonal-lattice SC with $m = 2$ and $n = 33$.

Fig. 2 shows the first steps of the top-down iterative process to generate SCs with different dimensions. Four steps $m = 1, \ldots, 4$ of the iteration are shown. Black squares corresponds to regions removed from of an initial square. Panel a) corresponds to $\mathcal{N} = 8$ and $\mathcal{L} = 3$ with dimension $d_{\rm H} = 1.89$. b) corresponds to $\mathcal{N} = 12$ and $\mathcal{L} = 4$ with dimension $d_{\rm H} = 1.79$.

Density-of-states

For small systems, the density-of-states is obtained by exactly calculating the Hamiltonian eigenvalues. For large systems with more than 10^5 sites, we use the tight-binding propagation method (TBPM) [1, 2]. Here, the DOS is obtained by the following Fourier transform [1–3]

$$\nu(E) = \frac{1}{2\pi} \int_{-\infty}^{\infty} \exp\left(iE\tau/\hbar\right) \langle\varphi|\varphi(\tau)\rangle \, d\tau \ , \qquad (1)$$

where $|\varphi\rangle$ is a random superposition of all the basis states in real space, i.e. $|\varphi\rangle = \sum_i a_i |i\rangle$, and a_i are random complex numbers normalized as $\sum_i |a_i|^2 = 1$. The wave propagation $|\varphi(\tau)\rangle \equiv \exp\left(-i\mathcal{H}\tau/\hbar\right)|\varphi\rangle$ is performed numerically by using the Chebyshev polynomial algorithm.

Fig. 3 shows the density-of-states of the tight-binding Hamiltonian (1) in the main text, for different lattice geometries: a) triangular, with $m = 4$ and $n = 284$ b) square, with $m = 4$ and $n = 162$, and c) hexagonal, with $m = 4$ and $n = 284$. All data correspond to SCs with $\mathcal{N} = 8$ and $\mathcal{L} = 3$.

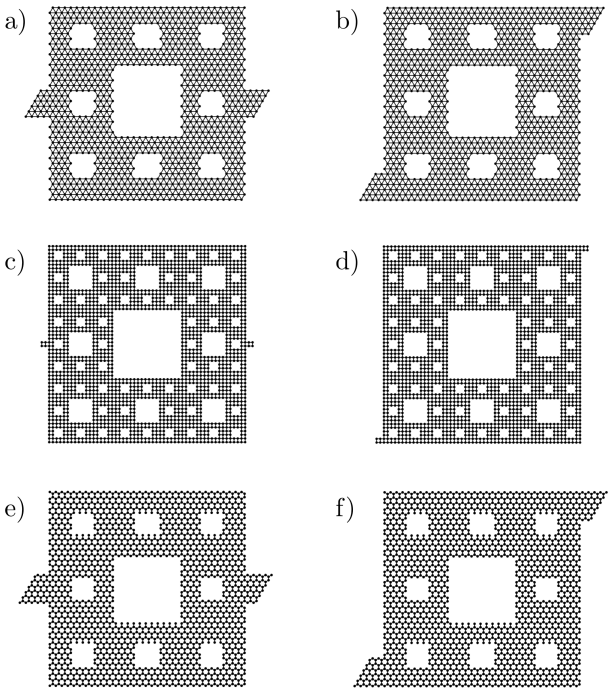

FIG. 1. SCs with triangular [a) and b)], square [c) and d)], and hexagonal [e) and f)] underlying lattices for central [a), c), and e)] and diagonal [b), d), and f)] lead positions.

Because of the absence of translational invariance, it is not possible to represent the eigenvalues of the Hamiltonian in terms of a conventional "band structure diagram". A few general observations can still be made on the spectrum of the Hamiltonian. On the square lattice, the Hamiltonian is particle-hole symmetric and the spectrum of eigenvalues extends from $-4t$ to $4t$ for a bandwidth equal to $8t$. The Hamiltonian on the honeycomb lattice is also particle-hole symmetric, and its eigenvalues range from $-3t$ to $3t$. Notably, the density-of-states does *not* display a gap in this case, but instead a edge state peak at $E = 0$. This is at odds with the case of antidot lattices created by piercing a hexagonal lattice with regularly spaced holes [4], where a gap is opened up

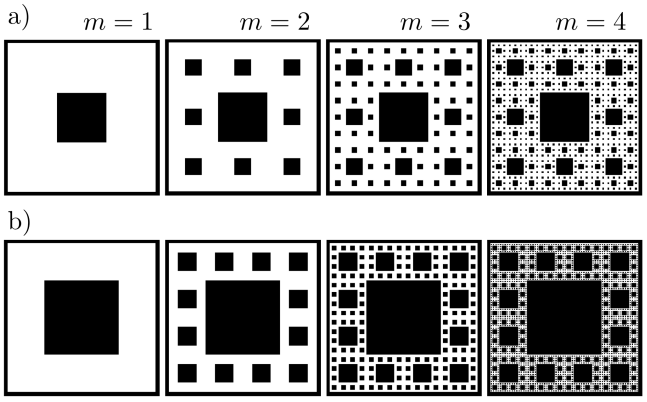

FIG. 2. Construction of SCs with different Hausdorff dimensions: a) $d_{\rm H} = 1.89$ and b) $d_{\rm H} = 1.79$. The black squares represent regions that are removed from the white sample. Four steps $m = 1, \ldots, 4$ of the iterative construction are shown.

in the well-known graphene-like linear-in-energy density-of-states. On the triangular lattice, eigenenergies range from $-6t$ to $3t$.

Persistence of conductive states in disordered square-lattice SCs

Fig. 4a) shows the energy dependence of the conductance $G(E)$ (in units of e^2/h) of a square-lattice SC in the presence of localized elastic disorder. A single-site vacancy is created along the path of the conductive state shown in Fig. 1e) in the main text, on the site of the SC with spatial coordinates $\boldsymbol{r}_i = (10, 18)$. We see that, despite such a strong, localized disorder source, $G(E)$ still reaches its maximum value $G(E) = 4e^2/h$ at $E = 0$.

Fig. 4b) shows $G(E)$ in the presence of smooth elastic disorder. The following potential term has been added to the Hamiltonian, Eq. (1) of the main text:

$$V = \sum_{i,\sigma} \delta\mu(\boldsymbol{r}_i) c^\dagger_{i,\sigma} c_{i,\sigma} \ . \qquad (2)$$

The profile $\mu(\boldsymbol{r}_i)$, shown in Fig. 4c), varies on a substantial energy scale, fixed to 20% of the hopping amplitude. The colorscale in Fig. 4c) varies from $-0.1t$ (blue) to $+0.1t$ (red). Fig. 4d) shows the conductive eigenstate at $E = -0.063t$ in the presence of the disorder potential. When confronted to the conductive bulk path in the absence of disorder, shown in Fig. 1e) of the main text, we see that the profile of the eigenstate is surprisingly robust. More precisely, we notice a weak ibridization with localized wavefunctions at the corners of the SC, but the main bulk paths of the unperturbed conductive wavefunction are clearly visible and connect the left and right side of the SC, where the leads are located. This explains

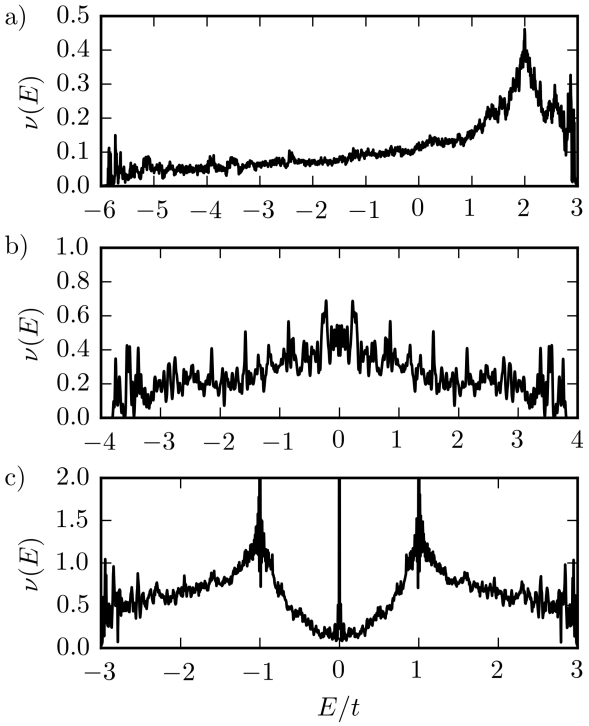

FIG. 3. Density-of-states of SCs with different underlying lattices: a) triangular, b) square, and c) hexagonal.

why the conductance around $E = -0.063t$ [indicated by a red arrow in b)] almost reaches its maximum value. We conclude that the conductance of the 2DEG in a SC is robust with respect to both localized and smooth elastic disorder.

For a geometry with a smooth disorder potential varying on an energy scale up to 20% of the hopping amplitude, we have verified that the conductance fluctuations display a fractal dimension which is comparable to that in the clean SC and is weakly dependent on the strength of the potential.

Box-counting algorithm applied to SCs with lower dimensions

Fig. 5 shows the results of the box-counting (BC) algorithm applied to square-lattice SCs with lower dimensions, which are obtained by increasing $\mathcal{L}$ and $\mathcal{N}$. This figure complements Fig. 2c) of the main text. The technical difficulty of obtaining this data is that the total number of sites in the sample increases as its dimension decreases, so that the calculation carries an increasing numerical burden.

The parameters of the SCs are: a) $\mathcal{N} = 12$, $\mathcal{L} = 4$, $m = 4$, and $n = 512$; b) $\mathcal{N} = 16$, $\mathcal{L} = 5$, $m = 4$, and

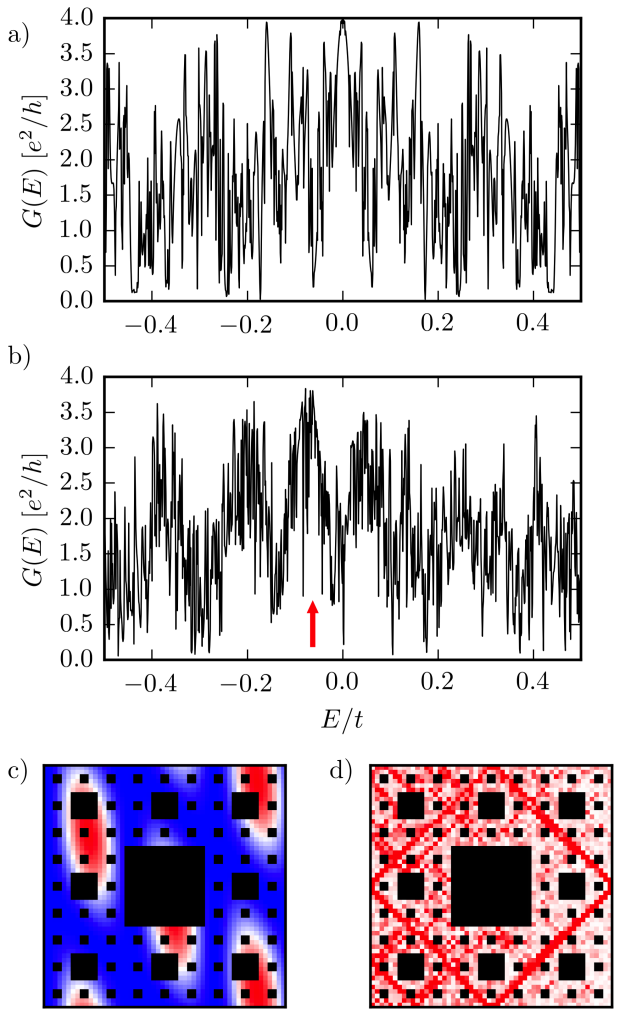

FIG. 4. (Color online) Quantum transport in a disordered SC. a) energy dependence of the conductance $G(E)$ (in units of e^2/h) of a square-lattice SC, in the presence of a single-site vacancy on the site of the SC with spatial coordinates $\boldsymbol{r}_i = (10, 18)$. b) $G(E)$ in the presence of the smooth elastic potential $\mu(\boldsymbol{r}_i)$ shown in c). The colorscale in c) varies from $-0.1t$ (blue) to $+0.1t$ (red). d) conductive eigenstate at energy $E = -0.063t$ [marked by the red arrow in b)] in the presence of the smooth elastic potential.

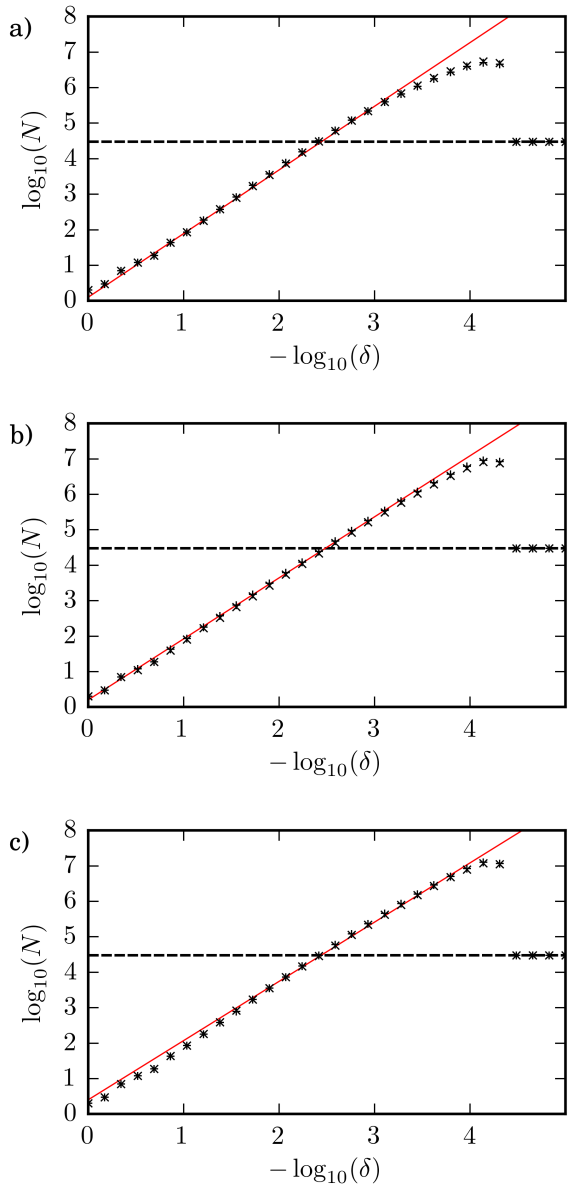

FIG. 5. (Color online) BC analysis of SCs with lower fractal dimensions: a) $d_{\rm H} = 1.79$, b) $d_{\rm H} = 1.72$, and c) $d_{\rm H} = 1.67$. Symbols + and × refer to central and diagonal lead positions, respectively. The horizontal dashed lines represent the saturation value $N = N_{\rm s}$, with $N_{\rm s} = 3 \times 10^4$. In each panel, the slope d of the solid line has been set equal to the Hausdorff dimension $d_{\rm H}$ of the SC.

$n = 1250$; c) $\mathcal{N} = 20$, $\mathcal{L} = 6$, $m = 4$, and $n = 2592$. In each panel, + and × symbols correspond to center and diagonal lead positions, respectively. The horizontal dashed lines represent the constant value $N = N_{\rm s}$, with $N_{\rm s} = 3 \times 10^4$. The slope d of the red solid lines has been set equal to the dimension $d_{\rm H}$ of the corresponding SC: a) $d = 1.79$; b) $d = 1.72$; and c) $d = 1.67$.

In each case, the BC algorithm displays a scaling region which exceeds two orders of magnitude, with a very clear scaling $N \sim \delta^{-d}$. This shows that the fractal nature of the conductance fluctuation persists also when the dimension of the SC is lowered. Moreover, the steepness of the data in the scaling region compares extremely well with the steepness of the line corresponding to the dimension $d_{\rm H}$ of the sample. This results support our conjecture that $d = d_{\rm H}$.

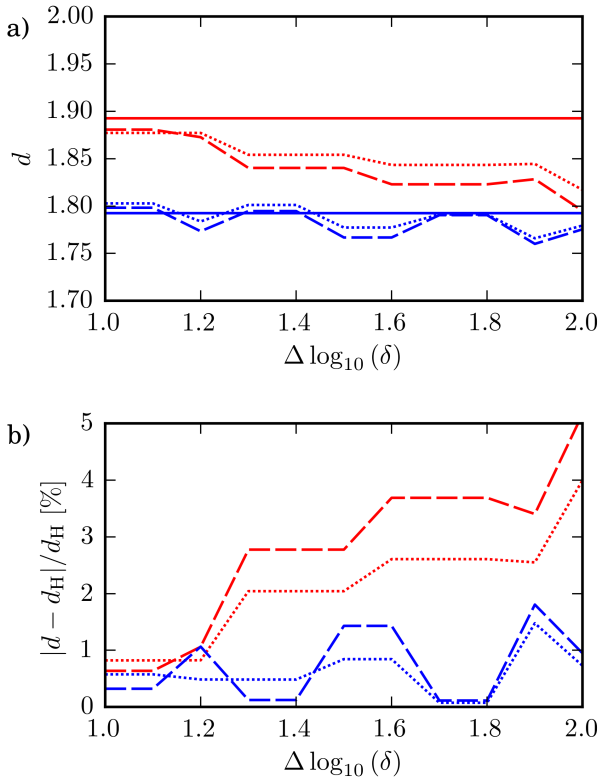

FIG. 6. (Color online) Estimation of the fractal dimension from the BC analysis. a) BC dimension d as a function of the extent $\Delta \log_{10}(\delta)$ of the interval where the linear fit to the BC data is calculated. b) relative difference between the calculated BC dimension d and the expected value $d_{\rm H}$.

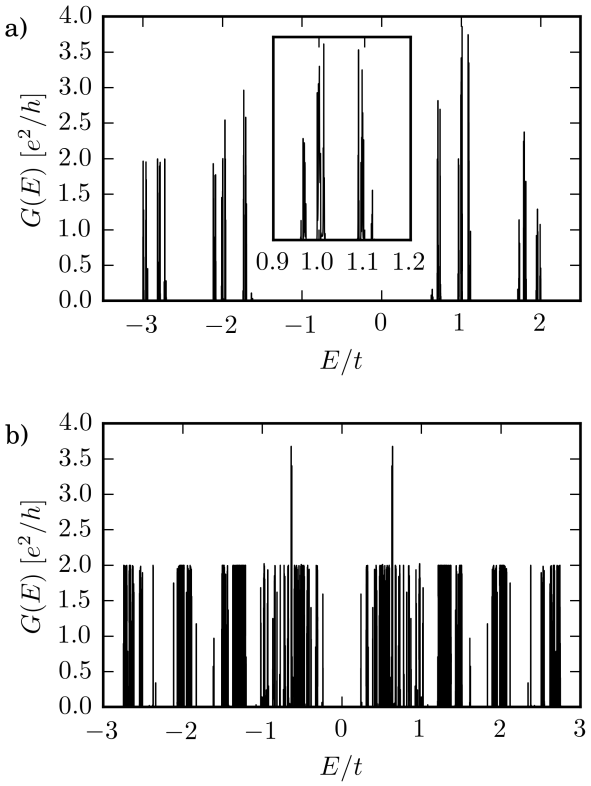

FIG. 7. Energy dependence of the conductance $G(E)$ (in units of e^2/h) for: a) the Sierpinski gasket and b) the Vicsek fractal. The inset in a) shows a magnification of the cluster of peaks around $E/t \sim 1$.

Estimation of the BC dimension

Fig. 6 details how the data from the BC algorithm are used to calculate the BC dimension d which is shown in Fig. 2d) of the main text. The BC algorithm is explained in the main text. Our estimate for the BC dimension is obtained by a best-fit procedure to the set of points $(-\log_{10}(\delta), \log_{10}(N))$ given by the BC algorithm. Here, N is the number of boxes of size δ needed to cover the graph of a conductance fluctuation curve. We point out that we always rescale the conductance curves to the unit square $[0,1] \times [0,1]$ before the analysis is applied.

The linear fit to the data is performed in an interval centered in the scaling region. The extent $\Delta \log_{10}(\delta)$ of the fitting interval is then changed to provide several different best-fit results. The whole scaling region has an extent $\Delta \log_{10}(\delta) \simeq 2.5$. The results presented in Fig. 2d) of the main text correspond to the average of the values d as the extent of the fitting interval is changed.

Panel a) shows the BC dimension d as a function of the extent $\Delta \log_{10}(\delta)$ of the interval where the linear fit is calculated. b) shows the relative difference between the calculated BC dimension d and the expected value $d_{\rm H}$. In both panels, red (blue) data corresponds to $\mathcal{N} = 8$ and $\mathcal{L} = 3$ ($\mathcal{N} = 12$ and $\mathcal{L} = 4$) with $m = 4$ and $n = 162$ ($n = 512$). Dashed and dotted lines correspond to center and diagonal lead positions, respectively. The red (blue) solid lines in a) correspond to the conjectured value $d_{\rm H} = 1.89$ ($d_{\rm H} = 1.79$).

The result of the linear fit is very robust as we change the extent of the fitting interval to cover the entire scaling region, over almost three orders of magnitude. The estimate of the dimension obtained with the linear fit matches the expected value $d_{\rm H}$ (i.e. the dimension of the SC) with an accuracy of a few percent in the whole scaling region.

Sierpinski gasket and Vicsek fractal

Fig. 7 shows the energy dependence of the conductance $G(E)$ for two fractals which do not belong to the family

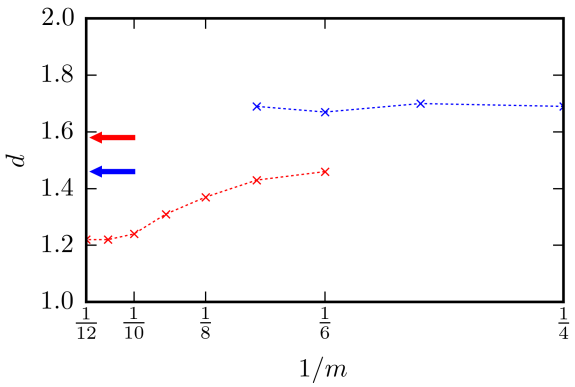

FIG. 8. (Color online) Finite-size scaling of the fractal dimension for the Sierpinski gasket and the Vicsek fractal. The symbols show the BC dimension d of the gasket (red) and Vicsek fractal (blue) as the number m of iterations in the generation of the fractal is increased. The dotted lines are guides to the eye. The red and blue arrow mark the values of the Hausdorff dimension $d_{\rm H} = 1.58$ and $d_{\rm H} = 1.46$ of the gasket and Vicsek fractal, respectively.

of SCs, i.e. the Sierpinski gasket and the Vicsek fractal, shown in Fig. 4a) and b) of the main text, respectively. a) shows the conductance for a gasket with $m = 8$ and $n = 256$; b) shows the conductance for a Vicsek fractal with $m = 6$ and $n = 1458$. We notice that the profile of the conductance is characterized by many intervals where the conductance vanishes. This behavior is in contrast to the conductance of the SC, which is non-zero in a broad energy support. The intervals of vanishing conductance do not appear to have a characteristic width nor a typical spacing, as is the case in a standard band structure. On the contrary, their structure is reminiscent of a self-similar geometry, as suggested by the inset of a), where it is seen that the conductance in the interval $0.9 < E/t < 1.2$ features four cluster of peaks, as in the whole interval $-3 < E/t < 2$. The self-similarity of the conductance graph is demonstrated by applying the BC algorithm, as shown in Fig. 4 of the main text, which yields a non-integer dimension d.

Fig. 8 shows the BC dimension d for the conductance fluctuations of the gasket (red) and Vicsek fractal (blue) as the number m of iterations in the generation of the fractal is increased. [Note that the m axis is nonlinear and, as customary for finite-size scaling analysis, shows $1/m$.] The crosses show the result of the BC analyses, the dotted lines are a guide to the eye, and the arrows mark the values of the Hausdorff dimension $d_{\rm H} = 1.58$ and $d_{\rm H} = 1.46$ of the gasket and Vicsek fractal, respectively. The figure shows that the estimate of d for the gasket is largely independent of m, and that convergence is achieved for the Vicsek fractal when $m \gtrsim 10$. In both cases, the estimated BC dimension d is substantially different than the Hausdorff dimension $d_{\rm H}$. More precisely $|d - d_{\rm H}| \gtrsim 10\%$ for the gasket and Vicsek fractal, while $|d - d_{\rm H}| \lesssim 2\%$ for the SCs, as shown in Fig. 6.

[1] S. Yuan, H. De Raedt, and M.I. Katsnelson, Phys. Rev. B **82**, 115448 (2010).

[2] S. Yuan, R. Roldán, H. De Raedt, and M.I. Katsnelson, Phys. Rev. B **84**, 195418 (2011).

[3] A. Hams and H. De Raedt, Phys. Rev. E **62**, 4365 (2000).

[4] T.G. Pedersen, C. Flindt, J. Pedersen, N.A. Mortensen, A.-P. Jauho, and K. Pedersen, Phys. Rev. Lett. **100**, 136804 (2008).